ADVANCED ENERGY MATERIALS
www.advenergymat.de

Tackling P3HT:Y-Series Miscibility Through Advanced Processing for Tunable Aggregation

*Fabian Eller, Christopher R. McNeill, and Eva M. Herzig**

Polymer and small molecule blend thin films are of strong interest for organic electronics and particularly organic solar cells. The high miscibility in blends of ordinary P3HT and state-of-the-art Y-series non-fullerene acceptors (NFAs) suppresses phase separation and aggregation challenging successful charge separation and transport. In a recent work, current-induced doping (CID) is introduced, a method to precisely control the aggregation of Poly(3-hexylthiophene) (P3HT) in solution. The highly ordered pre-aggregation in solution is used here to control the P3HT aggregation in neat films and blends with Y12 (BTP-4F-12). This results in a 25-fold increase in hole mobility in P3HT organic field-effect transistor (OFET) devices and tunability of the P3HT aggregate quality in the presence of Y12 over large ranges. At the same time, particularly the Y12 long-range ordering is heavily suppressed by increasing P3HT aggregation. However, solvent vapor annealing (SVA) leads to an extraordinarily high Y12 ordering, changes in the crystal orientation of Y12, and a further improvement of P3HT aggregation. A broad range of different degrees of aggregation of both materials can therefore be obtained in the final thin films solely by changing processing parameters without changing the composition of the material system.

1. Introduction

The introduction of Y-series non-fullerene acceptors (NFAs) like Y6, Y7, Y12, or others in the field of organic photovoltaics (OPV) led to a boost in power conversion efficiency (PCE) in combination with donor-acceptor copolymers like PM6.[1,2] Historically P3HT played an important role in OPV research, due to its simple and cheap synthesis and its high stability, making it still an attractive material.[3–11] However, in recent years it received less attention due to inherently low OPV efficiencies with most Y-series NFAs.[10,12,13] One reason is the lower open circuit voltage (V_{oc}) compared to, e.g., PM6 due to the higher HOMO of P3HT[12,14,15] and the higher energetic disorder of the Y-series NFA in P3HT than in, e.g., PM6,[16,17] but the detrimental problem is the high miscibility between P3HT and Y-series NFAs, which prevents the necessary phase separation for charge separation and transport.[10,12,18] With ZY-4Cl a Y-series NFA was explicitly designed to reduce the miscibility with P3HT, enabling a PCE of ≈10%.[11,18–20] Thus, chemical modification of NFAs is one possibility to achieve phase separation. Here we demonstrate that applying a new technique called current-induced doping (CID)[21] to obtain high-quality P3HT aggregates in solution can improve the P3HT aggregation in dried thin films with and without a second component present and hence causing an effective phase separation in an otherwise miscible material system.

During a CID treatment strong, electrical currents in the form of spark discharges between two tungsten electrodes immersed into the P3HT solution lead to a temporary doping of P3HT, which in turn results in aggregation. In our previous work, we demonstrated that the CID treatment allows unprecedented control over the aggregate fraction and quality of backbone ordering in solution.[21] The number of treatment steps and the strength of the treatment are two parameters to control the aggregation in solution, which are directly related to the CID treatment. Moreover, the solvent as well as concentration, and especially the temperature during treatment play an important role.[21]

We want to investigate the influence of the CID treatment on the film formation of neat P3HT and especially on blends with Y12, a highly miscible Y-series NFA with alkyl chains identical to ZY-4Cl. To control the aggregate fraction in the solution prior to casting the films, we varied the number of CID steps.

In the first part of this study, we examine aggregation control of neat P3HT films and the effect on organic field-effect transistor (OFET) devices. In the second part, we add untreated Y12 solution to CID-treated P3HT solution to blade-coat thin films and exploit solvent vapor annealing (SVA) to demonstrate tunable aggregation within both materials. Overall this approach only relies

F. Eller, E. M. Herzig
Dynamics and Structure Formation – Herzig Group
University of Bayreuth
Universitätsstraße 30, 95447 Bayreuth, Germany
E-mail: eva.herzig@uni-bayreuth.de
C. R. McNeill
Department of Materials Science and Engineering
Monash University
Wellington Road, Clayton, Victoria 3800, Australia

The ORCID identification number(s) for the author(s) of this article can be found under https://doi.org/10.1002/aenm.202304455

DOI: 10.1002/aenm.202304455

on processing parameters alone while conventional approaches to tune aggregation properties in thin films rely on the addition of extra components like high boiling point solvents,[22–24] dopants,[25–28] or changing solvents.[29–35]

2. Results and Discussion

2.1. Increasing Backbone Planarity in neat P3HT Films using CID Treatment

Current-induced doping (CID) allows us to produce solutions with different aggregate fractions with highly ordered P3HT aggregates. Further aggregation will take place upon drying such a solution to obtain thin films.

In **Figure 1a** absorption spectra of dried neat P3HT films with an increasing number of CID treatment steps (yellow to purple) are displayed. A particularly strong spectral change can be seen between the dried P3HT film without CID treatment (yellow) and the film with 1 CID treatment step. Despite the small amount of highly ordered aggregates with 1 CID step before coating (aggregate fraction of only ≈8% in Figure 1c), we observe a strongly increased A_1/A_2 ratio in the film (Figure 1d) accompanied by a redshift of the A_1 peak position (Figure 1b). These trends continue with an increasing number of CID steps finally reaching in the saturated regime an A_1/A_2 ratio of 0.85 and a peak position of 2.015 eV (redshift of 12 meV), which are both clear signs for a strong increase of backbone planarity.[36–41]

In general, aggregation in drying thin films starts upon reaching a critical concentration.[42] Examining the temporal evolution of the aggregate fraction for different CID treatment steps, allows us to investigate the effect of the presence of highly ordered aggregates in solution. The comparison of the slope of the temporal evolution of the aggregate fraction obtained from time-resolved in situ UV–vis spectroscopy during drying of blade coated thin films is therefore plotted without CID treatment and with 1 CID treatment step in Figure 1e. If no highly ordered aggregates are present (no CID treatment), the aggregation takes place within a well-defined, short time. The presence of highly ordered aggregates (with CID treatment) leads to a slow, systematic increase in aggregate fraction already in the wet film prior to the fast aggregation that occurs after reaching the critical concentration.

Combining the information from the temporal evolution with the strong increase of the backbone planarity from no solution treatment to a single CID step (Figure 1d) demonstrates that the aggregation process during drying is altered by the presence of the high-quality aggregates in solution, suggesting that these act as nuclei for further highly ordered aggregation.

Comparing grazing incidence wide angle X-ray scattering (GIWAXS) cake cuts of a dry samples without CID treatment and a strong treatment of 45 CID steps in Figure 1g–j shows that the scattering intensity of the lamellar stacking peaks (100), (200), and (300) is strongly increased in the vertical (out of plane, OOP) direction, while the (100) peak in the horizontal (in plane, IP) direction is significantly reduced. Both aspects lead to a strongly increasing ratio between the (100) OOP to IP amplitudes from 60 to 420 (increase by a factor of 7), demonstrating an increasing edge-on character (Figure S1, Supporting Information). Moreover, mixed index peaks like the (11*l*) and (012) (peaks shown in Figure 1h,j) at ≈1.24 and 1.87 $Å^{-1}$ respectively) become more prominent, which is a clear sign that aggregates are highly ordered in all three crystallographic directions.

Highly ordered aggregates with a highly planarized backbone and a strong edge-on character are ideal conditions for improving in-plane charge transport as required in OFET device geometries. Hole mobilities in the saturation regime of OFETs show this expected strong increase (Figure 1f, Figure S3,S4, Supporting Information). As in the UV–vis data, we also see here a particularly strong impact of the first CID step leading to an immediate, tenfold increase of the mobility demonstrating the importance of the function of the highly ordered aggregates as nuclei for aggregation. Equally in accordance with the UV–vis data, a saturation in mobility sets in with a final mobility increase of a factor of 25 compared to no treatment. Applying thermal annealing does not alter the mobilities and repeated measurements after storage in the glovebox for five weeks do not show any significant changes in the mobilities (see Figure S2, Supporting Information).

Hence, we have demonstrated that applying CID treatment to P3HT solutions allows us to obtain highly ordered aggregates in edge-on configuration in blade-coated P3HT thin films with highly improved charge transport properties solely by changing processing conditions without changing solvents, composition, or usage of additives.

2.2. Deliberate Enhancement and Suppression of Aggregation Behavior in Blend Films

For energy materials not only neat films are of interest but also nanostructural control in blended systems. In OPV the domain sizes of the blended material and the nanostructure of the components within these domains are decisive for charge separation and transport. In the following, we show that using CID on P3HT solutions we particularly tune the aggregate properties of P3HT in the resulting blend thin film, while using solvent vapor annealing after coating we dominantly enhance the aggregation behavior of the small molecule acceptor.

2.2.1. Enhancing P3HT Aggregation in as Cast Blend Thin Films Using CID Treatment

First, we examine the highly miscible blend of P3HT and the NFA Y12. Without any CID treatment, the UV–vis spectrum of the dried thin film is dominated by a very broad absorption peak ≈2.4 eV (red data in **Figure 2a**). In this peak, no vibronic shoulders are discernible, which is in contrast to the separated vibronic shoulders observed for neat P3HT (Figure 1a) or also in blends with many other acceptors (e.g., EH-IDTBR in Figure S5, Supporting Information). The addition of Y12 to P3HT therefore results in an increased energetic disorder, broadening the single peaks in the vibronic structure to an extent that these are no longer discernible. The behavior of the Y12 in the identical drying process in the low energy range of the in situ spectra in Figure 2a shows a clearly blueshifted absorption maximum in comparison to PM6:Y12 blends, and an even stronger blueshift for neat Y12 (see Figure S6, Supporting Information). This indicates an increased disorder not only for P3HT but also of the Y12 in the P3HT:Y12 blend, confirming the miscibility of the two materials.

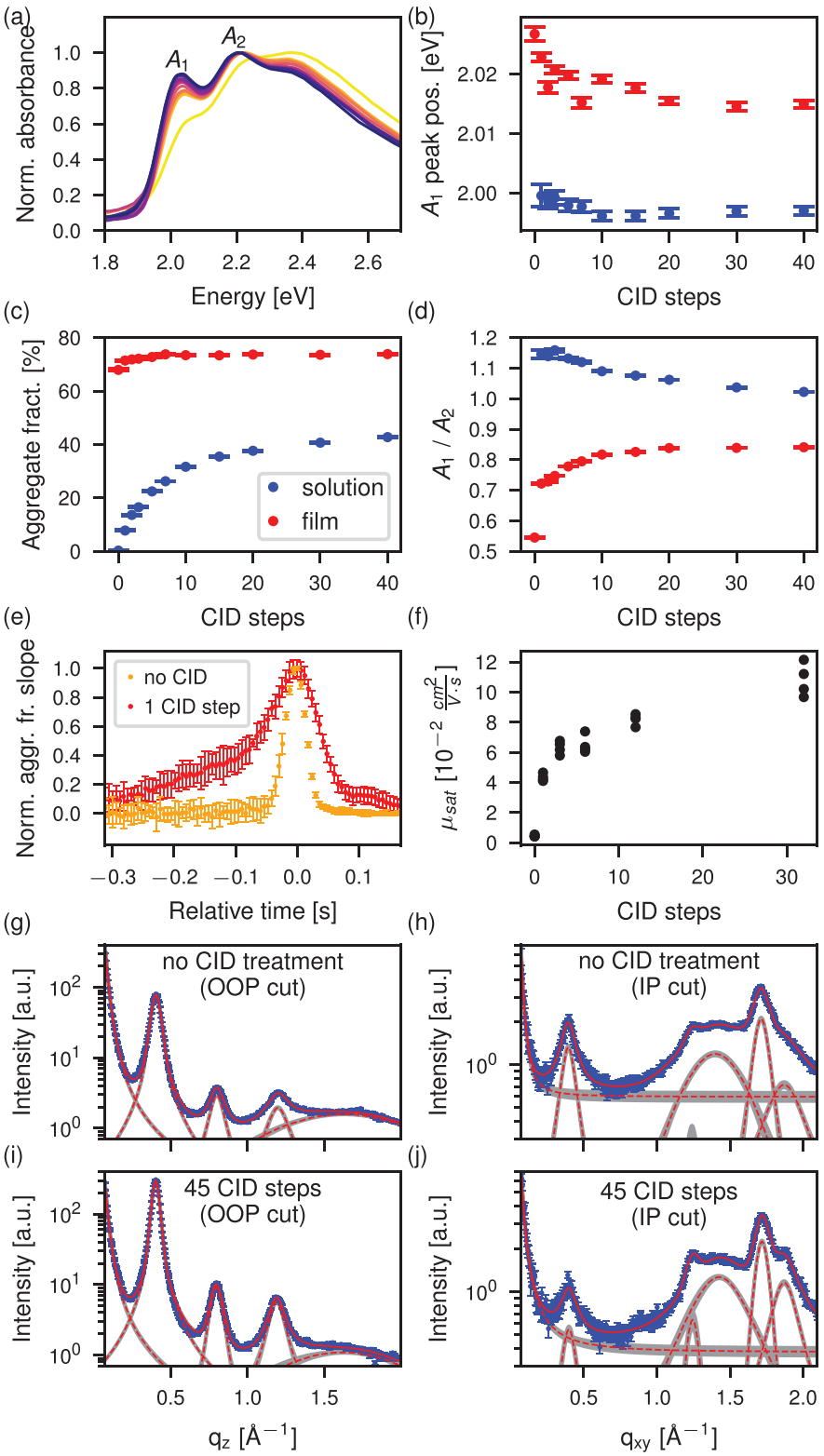

Figure 1. a) Normalized UV–vis absorption spectra of dry P3HT with an increasing number of CID steps (from yellow (untreated) to purple (45 CID steps)). b)-d) Results of fitting the vibronic structure in the dry film spectra (red) from a) and the respective solution spectra (blue) before drying: b) A_1 peaks position, c) minimum aggregate fraction, and d) ratio between peak amplitudes of the A_1 to A_2 peak. e) Normalized slope of the temporal evolution of the aggregate fraction during drying without CID treatment and with 1 CID step. f) Hole mobility in the saturation regime of bottom-contact bottom-gate field effect transistors. g)-j) Vertical (OOP) and horizontal (IP) cake cuts (blue) with fits (red) and 1σ confidence intervals (grey) of P3HT g), h) without CID treatment and i), j) with 45 CID steps.

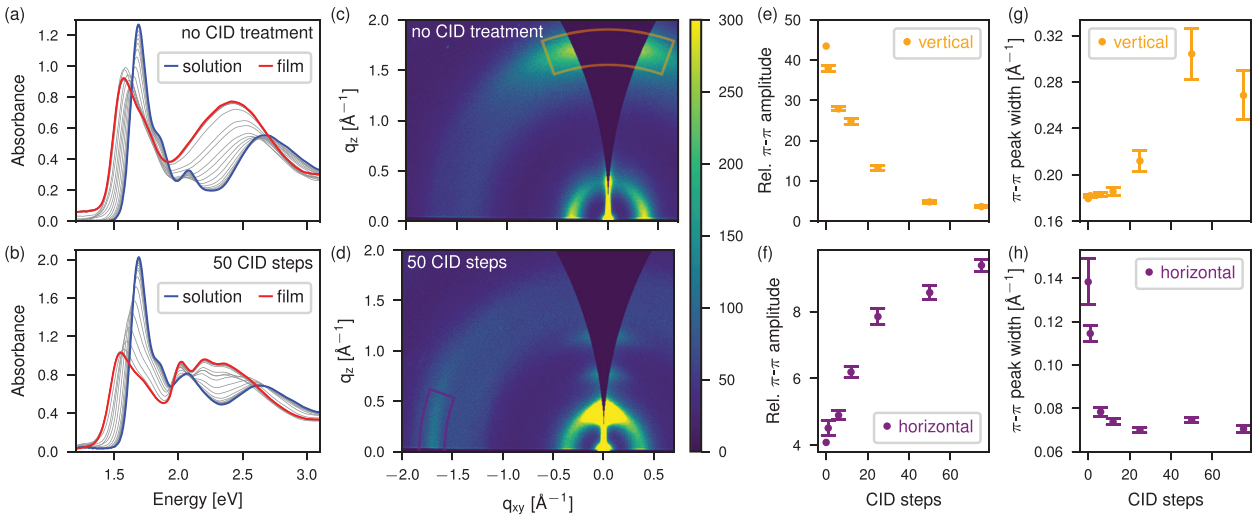

Figure 2. In situ UV–vis absorption spectra during the drying of 16.5 mg mL^{-1} P3HT:Y12 solutions: a) without CID treatment and b) with 50 CID steps. c), d) 2D GIWAXS data of P3HT:Y12 films: c) without CID treatment and d) with 50 CID steps. e–h) π–π amplitudes relative to the disordered ring at ≈1.4 Å^{-1} and π–π peak widths from fitting vertical and horizontal cake cuts.

For increasing numbers of CID steps **Figure** 3d shows a stronger suppression of the overall Y12 oscillator strength. This can be explained by a reduction of the in-plane orientation of the Y12 transition dipole moments since we are probing with light of normal incidence which couples to the in-plane components of the transition dipole moments. The loss of in-plane orientation of Y12 is linked to the loss of face-on orientation as shown in GIWAXS measurements in Figure 2c,d, and discussed below. At the same time, the CID treatment induces a very clear P3HT vibronic structure within the final film (Figure 2b). The vibronic structure is already present in the solution before drying (blue curve in Figure 2b and Eller et. al.[21]), but due to the superposition of a

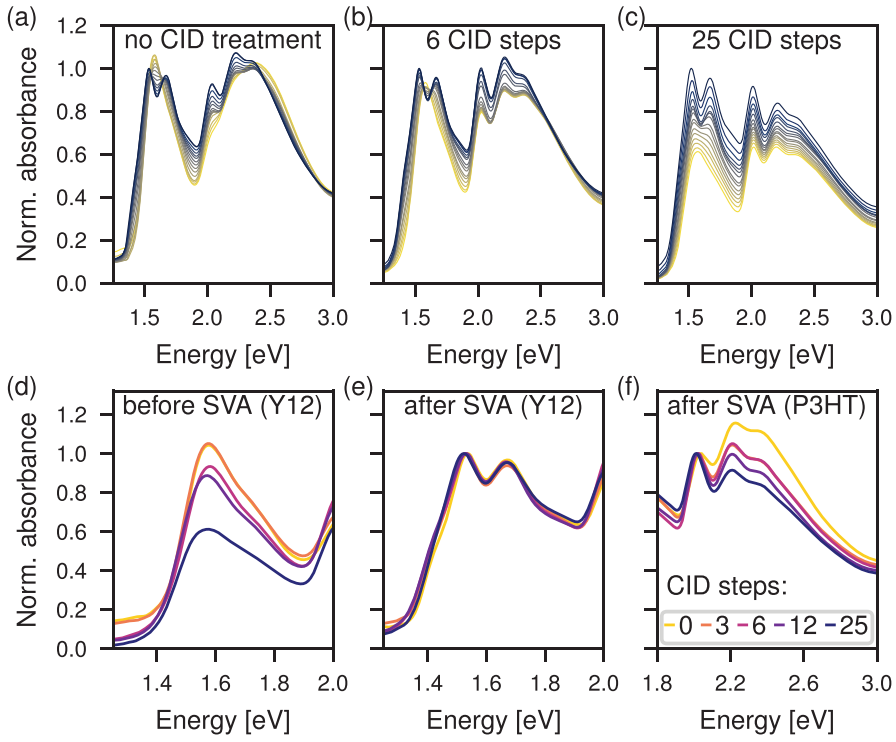

Figure 3. In situ UV–vis absorption spectra of P3HT:Y12 films: a) without CID treatment, b) with 6 CID steps, c) with 25 CID steps during SVA in a saturated toluene atmosphere (yellow before SVA, black after SVA). d–f) Comparison of absorption spectra with different numbers of CID steps: d) before SVA and e), f) after SVA. The spectra in a)-e) are normalized to the Y12 peak absorbance at the end of the SVA, while in f) the spectra are normalized to the P3HT A_1 peak after SVA.

Y12 peak at ≈2.1 eV, no separation of the A_1 and A_2 vibronic peak is discernible. During drying further highly ordered aggregation of P3HT occurs, probably due to nucleation at the highly ordered aggregates from the CID treatment in solution (see temporal evolution of the P3HT absorbance change in Figure S7, Supporting Information).

For the discussion of the nanostructure in the examined thin films we differentiate between short- and long-range order. With UV–vis spectroscopy we probe interactions between chromophores and therefore access information on short-range interactions. Using GIWAXS we exploit interference effects of X-rays reradiated by the electrons of the molecular units in a particular arrangement. In analogy to a diffraction grating, we obtain information on the degree of structural order beyond neighboring molecular elements, hence on the long-range ordering within the film. The weak short-range ordering of P3HT in P3HT:Y12 blends without CID treatment implies no significant long-range ordering of P3HT. This conclusion is confirmed by the GIWAXS measurement in Figure 2c, which lacks clear scattering signals of long-range ordered P3HT. The relatively strong π–π peak in the vertical (marked by orange wedge) and the scattering signal ≈0.35 $Å^{-1}$ is typical for Y12 in polymer-Y12 blends (for reference Figure S8 (Supporting Information) GIWAXS measurements of neat Y12 and PM6:Y12). However, the peak widths of both these signals are larger than in a comparable PM6:Y12 blend (see Figure S8, Supporting Information) and no onset of the nanostructure scattering of the (110) and (011) Y12 peaks (corresponding crystal structure see 2.2.2) is detected, implying that the long-range ordering of Y12 is also reduced.

A strong ordering of P3HT, however, can now be induced in the dry blend film by CID treatment. GIWAXS data of samples with strong CID treatment (Figure 2d; Figure S9, Supporting Information) show that the P3HT signal dominates the scattering pattern. The P3HT lamellar peaks (100), (200), and (300) in the vertical and the π–π stacking in the horizontal (marked by purple wedge) are observed, while no discernible scattering of the Y12 nanostructure and its π–π peak is detected anymore. It appears that the P3HT solution pre-aggregation due to the CID treatment, followed by P3HT aggregation during drying, enables P3HT long-range ordering, but hinders at the same time the formation of Y12 long-range ordering (even more than without CID treatment). To track the rise of the P3HT and the decay of the Y12 long-range ordering, the π–π peak amplitudes (relative to the disordered ring at ≈1.4 $Å^{-1}$) and the peak widths of the π–π peaks in the vertical (OOP) and horizontal (IP) respectively are displayed in Figure 2e–h. Supported by the orientation of the neat materials, we attribute the OOP π–π peak to dominantly Y12 and the IP π–π peak to dominantly P3HT (see Figure S8, Supporting Information). The relative π–π amplitude of Y12 decays by a factor of ≈10 until it saturates at a low level, which may also partially stem from face-on oriented P3HT. The peak width slowly increases at low numbers of CID steps until a more drastic increase of the peak width indicates a highly disordered π–π structure of the Y12. The P3HT π–π stacking amplitude increases rapidly at low CID treatment steps and then increases more slowly, while the P3HT π–π peak width drops rapidly to a nearly constant level indicating a strongly increased long-range order of P3HT with CID treatment in the π–π stacking direction.

Furthermore, RSoXS (Resonant Soft X-ray Scattering) measurements in Figure S10 (Supporting Information) show an overall increase in scattering intensities with an increasing number of CID steps. This is consistent with an increase in domain purity. However, a more detailed interpretation is challenging since film thickness and roughness need also to be considered.

Overall, we have shown that drying CID-treated solutions allows us to systematically tune the P3HT aggregation in thin films as a function of the number of CID steps while suppressing Y12 structure formation.

2.2.2. Enhancing Small Molecule Acceptor Aggregation Using Solvent Vapor Annealing on Dry Blend Thin Films

For structural control of nanomorphology in a blended system, both components need to be accessible for tuning. We have shown that the CID treatment can control the aggregation behavior of P3HT. We therefore aim to address the small molecule acceptor using post-treatments. We tested the two most common post-processing techniques thermal annealing (TA) and solvent vapor annealing (SVA). Since the Y12 structure formation with CID treatment is heavily suppressed during drying, we need to ensure successful nucleation of Y12 in subsequent processing. Therefore, we choose a two-step TA approach, where a first short (5 min) annealing step at 90 °C (close to the transition temperature of Y12) should increase Y12 nucleation and a second longer (10 min) annealing step at 120 °C should enhance larger-scale aggregation.[43] Even though the Y12 absorption peak is redshifted to 1.508 eV (for comparison PM6:Y12 with the same treatment 1.512 eV), GIWAXS does not reveal a significant increase in long-range ordering (see Figure S11, Supporting Information). Mainly the P3HT contributions in the GIWAXS measurement shows a longer range of ordering by significantly decreased peak widths and increased peak amplitudes after TA.

We conducted SVA in a saturated toluene environment and tracked the UV–vis absorption during the SVA in situ, as it is displayed for different numbers of CID treatment steps in Figure 3a–c. We stopped the SVA treatment after 5 min for each sample when no more changes were detectable in the UV–vis spectra. The CID treatment and SVA strongly influence the Y12 aggregation behavior.

After SVA the reduced Y12 absorption observed after drying recovers and the absorption peaks are clearly separated. We associate these two peaks with the two aggregate species (aggregate I at lower and aggregate II at higher energy) identified in similar material systems (Y6 and N4 as NFAs differing only in alkyl sidechains) by Kroh et al.[44] We observe an increased order of Y12 after SVA obtained from the observed redshift of aggregate I and the reduction in peak width (see evolution during SVA in Figure 3a–c; values before and after SVA in Table S1, Supporting Information). Furthermore, we observe that there is no strong dependency on the number of CID treatment steps (Figure 3e, merely a slight increase of peak width in Table S1, Supporting Information), although the nanomorphology of the individual films prior to SVA is different. Thus, the Y12 absorption after SVA suggests, that Y12 strongly gains in ordering and in-plane orientation of the transition dipole moments upon SVA.

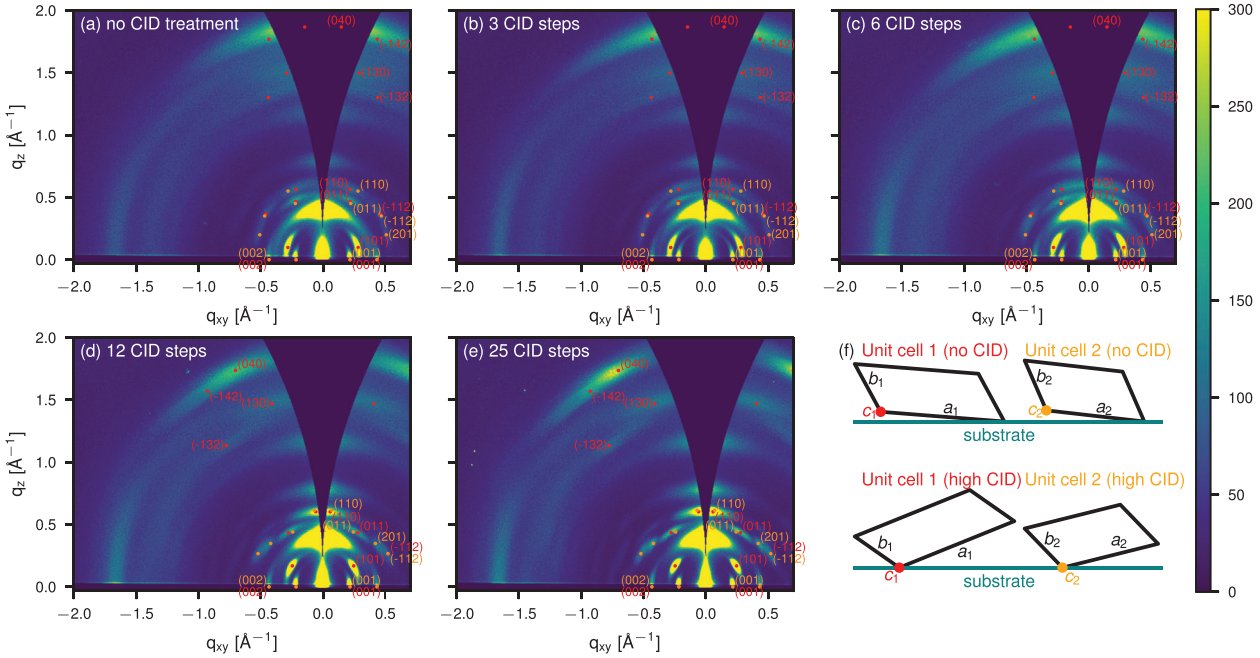

Figure 4. 2D GIWAXS data of P3HT:Y12: a) without CID treatment, b) with 3, c) 6, d) 12, and e) 25 CID steps all post-treated with SVA in a saturated toluene atmosphere. The lattice parameters of the Y12 unit cell 1 (peaks indexed in red) are $a_1 = 36.5$ Å, $b_1 = 16$ Å, $c_1 = 29$ Å, $\alpha_1 = 90°$, $\beta_1 = 90°$, $\gamma_1 = 123°$, and the lattice parameters of the Y12 unit cell 2 (peaks indexed in orange) are $a_2 = 29$ Å, $b_2 = 16$ Å, $c_2 = 29$ Å, $\alpha_2 = 90°$, $\beta_2 = 90°$, $\gamma_2 = 120°$. f) Sketch of side view of the two unit cells used for indexing showing the rotation around the c-axis. For up to 6 CID steps this is ≈4.5° for unit cell 1 and ≈6.5° for unit cell 2 (top row). From 12 CID steps onward the rotation around the c-axis is ≈−22° for unit cell 1 and ≈−14° for unit cell 2 (bottom row).

Examining the behavior of P3HT upon SVA, we see that especially without CID treatment an increase in P3HT ordering is apparent due to the increase of well-defined vibronic peaks in the UV–vis data (Figure 3a). The already well-defined vibronic structure due to the CID treatment in Figure 3b,c with 6 and 25 CID steps is further enhanced by the SVA annealing evident in the increase of the A_1/A_2 ratio. This control of P3HT backbone planarity due to the combination of CID treatment and SVA is particularly well observable when comparing the spectra after SVA normalized to the A_1 peak in Figure 3f.

Examining the long-range order of Y12 after SVA using GIWAXS (**Figure 4**, larger representation in Figures S12 and S13, Supporting Information) clearly demonstrates an increase for all starting conditions in line with the increase in short-range Y12 ordering as observed by UV–vis. All GIWAXS measurements show a rich Y12 nanostructure with low peak width in the radial direction (see Figure S14, Supporting Information, at a higher sample-to-detector distance with smaller footprint broadening). These observations allow the conclusion that the Y12, which was previously in a highly disordered intermixed phase, now forms domains with high purity consisting of highly ordered 3D nanostructures. While the peaks along q_{xy} without q_z-component ((001), (002), and (003)) are unchanged upon CID treatment, an increased number of CID steps leads to an azimuthal rotation of the remaining peaks without changes in the magnitude of q. To index all dominant peaks, two unit cells are required. Two unit cells also properly explain the observed (110) double peak at higher numbers of CID treatment steps (more details in Figure S15, Supporting Information). Optimizing the lattice parameters of both unit cells allows us to index all dominant Y12 peaks (Figure 4). It is possible to model the 2D GIWAXS data with any number of CID treatment steps with the identical two unit cells (marked red and orange in Figure 4 respectively), just by varying the rotational angle of the unit cells around the horizontal *c*-axis (thus varying the tilt of the crystal structures with respect to the substrate). Observing an unchanged unit cell structure for all SVA-treated films implies also no changes in the intermolecular arrangements in accordance with the nearly identical spectra obtained from UV–vis spectroscopy (Figure 3e). The optimized lattice parameters are $a_1 = 36.5$ Å, $b_1 = 16$ Å, $c_1 = 29$ Å, $\alpha_1 = 90°$, $\beta_1 = 90°$, $\gamma_1 = 123°$ for unit cell 1 and $a_2 = 29$ Å, $b_2 = 16$ Å, $c_2 = 29$ Å, $\alpha_2 = 90°$, $\beta_2 = 90°$, $\gamma_2 = 120°$ for unit cell 2.

Since all peaks in the measurements extend over a significant azimuthal range the values of rotations extracted for the two unit cells marked with the dots in the 2D images represent the dominant orientation but occur over a broader range of unit cell rotations. Initially, for no and up to 6 CID steps, the rotation around the *c*-axis is ≈4.5° for unit cell 1 and ≈6.5° for unit cell 2. From 12 CID steps onward the rotation around the *c*-axis is ≈−22° for unit cell 1 and ≈−14° for unit cell 2 (shown in Figure 4f). While the sample with 6 CID steps is similar to the two data sets in Figure 4a,b, i.e., dominated by unit cells that are weakly rotated, it also contains scattering intensities of the more strongly rotated unit cells observed for the higher numbers of CID steps (Figure 4d,e). In Tables S2 and S3 (Supporting Information) the values for q_{xy}, q_z, and q of all indexed peaks are displayed.

P3HT also responds to the SVA treatment with long-range ordering probed by GIWAXS. This response is particularly strong when there is no prior CID treatment, where significant edge-on aggregates are present after SVA (Figure 4a) in comparison

to no signature of aggregation of P3HT prior to SVA (Figure 2c). For the CID treated samples, a further improvement of the pre-existing P3HT aggregation occurs during SVA (direct comparison in Figure S16, Supporting Information) but keeping the increasing strength of long-range order as a function of CID treatment steps.

Overall, the SVA treatment dominantly addresses an improved ordering of the Y12 on the nanoscale with no negative impact on P3HT aggregation. We therefore have demonstrated that independent of the pre-condition of the P3HT matrix the Y12 can be strongly aggregated resulting in high-quality aggregates by application of SVA.

3. Conclusion

We have successfully demonstrated the opportunity of CID treatments on P3HT solutions for nanostructural control in thin films. We observe that the high tunability within the solution transfers to the neat thin films of P3HT leading to a 25-fold increase in OFET hole mobility. It is especially remarkable that already the first CID treatment step is sufficient to achieve a ten-fold increase demonstrating the great importance of the highly ordered aggregates produced by the CID treatment as nuclei for further aggregation.

Furthermore, we can use the CID treatment in combination with SVA to demonstrate unprecedented control over the aggregation behavior in the P3HT:Y12 blend. Using these processing approaches we can produce from the same solvent, without changing the composition or using additives, final films that are either highly disordered, show only order in the Y12 or P3HT alone, and also on the contrary highly ordered Y12 with different orientations of Y12 and different degree of order in P3HT. Moreover, our in situ UV–vis measurements during SVA suggest, that an intermediate range of Y12 ordering may be accessible by reducing the SVA time. This specific, almost separate control over the P3HT and Y12 ordering can be highly valuable for fundamental research. While transferring the mechanism of inducing aggregation via CID treatment to other polymeric materials is challenging, the choice of the NFA or additional components can be widely varied, since these materials are added after the CID treatment. Therefore, potential fundamental studies can include but are not limited to studies on charge transport, electron and hole mobility, energy levels, solar cell properties, stability, and trap densities all as a function of, e.g., the degree of aggregation or depending on crystal orientation. We are therefore convinced that CID-treated thin films will be helpful for further understanding and optimizing energy materials.

4. Experimental Section

Materials: P3HT with a regioregularity of 96% was purchased from Rieke Metals, Y12, PM6, and EH-IDTBR from Brilliant Matters, PEDOT:PSS (poly(3,4-ethylenedioxythiophene) polystyrene sulfonate) from Heraeus, chloroform from Sigma–Aldrich and toluene from VWR Chemicals. All materials were used as received.

CID Treatment: Since this work is interested to exploit highly ordered aggregates, chloroform as solvent was chosen at a temperature of 20 °C with a voltage of 300 V for charging the capacitor, which yielded the highest aggregate quality in this extensive previous study.[21] The untreated P3HT solutions were prepared by dissolving P3HT in chloroform at 50 °C for 20 min. Prior to the CID treatment, the solutions were kept for 15 min at 20 °C to allow for proper equilibration. This temperature was also kept constant throughout the complete CID treatment. A capacitor (WIMA MKS 4, 3.3 µF) was charged to 300 V and subsequently connected to two tungsten wires separated by several millimeters and immersed into the P3HT solution. These two tungsten wires were then approached until a spark discharge occurred below a separation of 1 mm. This procedure of charging the capacitor, connecting, and approaching the tungsten wires was repeated until the desired number of CID treatment steps was achieved.[21]

Sample Preparation: The glass and silicon substrates were cut to the desired size and then thoroughly cleaned by sonication in Alconox, VE-water, and isopropanol for 10 min each. To ensure a comparable surface all samples were spin–coated with sonicated PEDOT:PSS at 3000 rpm. The neat P3HT samples were coated from 12 mg mL^{-1} P3HT solutions treated with the given number of CID steps. For the P3HT:Y12 blends also 12 mg mL^{-1} P3HT solutions treated with the given number of CID steps were used and subsequently blended with 24 mg mL^{-1} Y12 solutions (without CID treatment) with a volume ratio of 5:3. Thus, the resulting mixing ratio of Y12 to P3HT was 1.2:1 and the concentration 16.5 mg mL^{-1}. All samples were coated with a home-built blade-coating setup at a coating speed of 10 mm s^{-1}. During every drying process on glass substrates the UV–vis absorption was tracked in situ.[45]

UV–Vis Absorption Spectroscopy: A combined deuterium and halogen white light source from Ocean Optics and an AvaSpec-HSC1024 × 58 TEC-EVO spectrometer from Avantes were used to acquire the in situ UV–vis spectra of the neat P3HT samples during drying. For the in situ drying measurements of the blend samples and the in situ SVA measurements, an AvaLight-HAL-S-Mini2 halogen white light source and an AvaSpec-ULS2048CL-EVO-RS-UA spectrometer (both from Avantes) were used. Amorphous P3HT spectra measured at the same concentration and temperature were scaled to the high-energy shoulder of the neat P3HT absorption spectra at ≥2.6 eV.[46,47] This rescaled amorphous spectrum was subsequently subtracted from the neat P3HT absorption spectrum, which was then fitted by the sum of five equidistant (distance of 0.17 eV between peaks) Gaussian peaks for the A_1 to A_5 peaks.[46,47] While an identical peak width was fitted for the A_2 to A_5 peaks, a smaller peak width was fitted for the A_1 peak.[48,49] The minimum aggregate fraction was calculated using the area below the fits and below the rescaled amorphous spectrum considering the different molar extinction coefficients of the amorphous and aggregated P3HT described by Clark et al.[46] This procedure yields an estimate for the minimum aggregate fraction as higher optical transitions of the aggregate could contribute to the high energy shoulder leading to an overestimation of the amorphous absorption.

The in situ absorption data showing the transition from liquid to solid film or the effect of SVA was chosen to display well the occurring changes and were not necessarily equidistant in time. To determine the slope of the aggregate fraction the difference of data points 30 ms apart is considered.

GIWAXS: Grazing incidence wide-angle X-ray scattering (GIWAXS) was performed on a laboratory system at the University of Bayreuth (Xeuss 3.0, Xenocs SAS, Grenoble, France) with a Cu Kα source (λ = 1.54 Å), a Dectris EIGER 2R 1 M detector, and a sample-to-detector distance of 72 mm (and 200 mm for the measurements in Figures S14 and S15, Supporting Information) and a beam size of 500 µm. The presented 2D data were wedge-corrected scattering images with solid angle correction. Scattering experiments were carried out at room temperature under vacuum on samples on PEDOT:PSS coated silicon substrates with a length of 5 mm in beam direction. The incident angle was set to 0.18° (above the critical angle of ≈0.16°), which probes the full depth of the films. The presented q-profiles were cake cuts covering an azimuthal angle of 70°–110° for the cuts in the vertical direction and 0–20° as well as 160°–180° for the cuts in the horizontal direction.

All fits to the cuts of the GIWAXS data were Pseudo-Voigt fits, described by the following expression for a single peak:

$$f\ (q) = A \cdot [\eta \cdot L\ (q) + (1 - \eta) \cdot G\ (q)]\ \textit{with}\ 0 < \eta < 1 \quad (1)$$

$$G\ (q) = exp\left[-ln\ (2) \cdot \left(\frac{q-c}{b}\right)^2\right],\ L\ (q) = \frac{1}{1+\left(\frac{q-c}{b}\right)^2} \quad (2)$$

where A is the peak amplitude, c is the peak position, $2b$ is the full width at half maximum (the obtained values for the peak width were the values of b) of the Pseudo-Voigt peak, and η the Pseudo-Voigt mixing parameter. To fit the superposition of various peaks, the sum of several Pseudo-Voigt peaks was fitted for both directions. Moreover, an additional background was fitted. It consists of a q^{-4} decay in the horizontal direction and a q^{-5} decay in the vertical direction with an additional q^{-2} decay and an offset in both directions.

To index the data a self-written Python program was used to calculate and superimpose the various peak positions on the original data. The program allows the rotation around individual crystal axes. In plane isotropy is assumed.

OFET-Device Fabrication and Characterization: Substrates for organic field-effect transistors with a bottom-gate bottom-contact (BGBC) geometry were purchased from Fraunhofer IPMS Dresden (OFET Gen. 4). Substrate and gate-electrode consisted of heavily n-doped silicon, while 230 nm of thermally grown silicon oxide was the gate dielectric ($C = 1.5 \times 10^{-8}$ F cm^{-2}). Interdigitated electrodes were patterned from gold (30 nm) and used as source- and drain-contacts, the used channel-widths were 20 µm. The substrates were thoroughly cleaned by sonication in isopropanol and acetone for 10 min each and the P3HT was deposited in the same way as the other films. No silanization or other surface treatment was used. Afterward, the devices were transferred into a nitrogen-filled glovebox and the transistor characteristics were measured using the Agilent Technologies B1500A Semiconductor Device Analyzer. The mobilities were extracted from the slope of the $I_D{}^{0.5}$ versus V_G-plots in the saturation regime, using:

$$I_D = \frac{W}{2L} \cdot \mu \cdot C \cdot (V_G - V_{Th})^2 \quad (3)$$

where I_D is the drain current, W the channel width, L the channel length, C the capacitance per unit area μ_{sat} the charge carrier mobility, V_G the gate voltage and V_{Th} the threshold voltage.[38]

RSoXS: Resonant Soft X-ray scattering (RSoXS) measurements were collected at the Spectroscopy Soft and Tender (SST-1) beamline at the National Synchrotron Light Source II.[50]

Measurements were carried out in vacuum with the incident beam normal to the substrate passing through the silicon nitride window prior to passing through the sample. Two-dimensional scattering patterns were recorded on a charge-coupled device (CCD) detector sensitive to soft X-rays (greateyes GmbH) at a sample-to-detector distance of 35 mm and a photon energy of 285.4 eV.

Supporting Information

Supporting Information is available from the Wiley Online Library or from the author.

Acknowledgements

F.E. and E.M.H. thank the Deutsche Forschungsgemeinschaft (DFG Research Unit FOR 5387 POPULAR, Project No. 461909888 and Project INST 91/443-1) for their support. This work was also supported by a Senior Research Fellowship (CRM) from the University of Bayreuth Centre of International Excellence "Alexander von Humboldt".The authors are grateful to Florian Meichsner (Macromolecular Chemistry, University of Bayreuth) for the introduction and support with the OFET measurements and analysis and to Eliot Gann (Brookhaven National Laboratory) and Priyanka M. Ketkar (National Institute of Standards and Technology) for help with the RSoXS measurements. This research used the Spectroscopy Soft and Tender (SST-1) beamline of the National Synchrotron Light Source II, a U.S. Department of Energy (DOE) Office of Science User Facility operated for the DOE Office of Science by Brookhaven National Laboratory under Contract No. DE-SC0012704.

Open access funding enabled and organized by Projekt DEAL.

Conflict of Interest

The authors declare no conflict of interest.

Data Availability Statement

The data that support the findings of this study are available from the corresponding author upon reasonable request.

Keywords

current induced doping, GIWAXS, morphology, nanostructure, NFA, solvent vapor annealing, UV–vis spectroscopy

Received: December 22, 2023
Revised: March 29, 2024
Published online: May 19, 2024

[1] Q. He, P. Ufimkin, F. Aniés, X. Hu, P. Kafourou, M. Rimmele, C. L. Rapley, B. Ding, *SusMat* **2022**, *2*, 591.
[2] B. Lu, J. Wang, Z. Zhang, J. Wang, X. Yuan, Y. Ding, Y. Wang, Y. Yao, *Nano Select* **2021**, *2*, 2029.
[3] J. H. Bannock, S. H. Krishnadasan, A. M. Nightingale, C. P. Yau, K. Khaw, D. Burkitt, J. J. M. Halls, M. Heeney, J. C. de Mello, *Adv Funct Mater* **2013**, *23*, 2123.
[4] D. Baran, R. S. Ashraf, D. A. Hanifi, M. Abdelsamie, N. Gasparini, J. A. Röhr, S. Holliday, A. Wadsworth, S. Lockett, M. Neophytou, C. J. Emmott, J. Nelson, C. J. Brabec, A. Amassian, A. Salleo, T. Kirchartz, J. R. Durrant, I. McCulloch, *Nature Mater* **2017**, *16*, 363.
[5] N. Chander, S. Singh, S. S. K. Iyer, *Sol. Energy Mater. Sol. Cells* **2017**, *161*, 407.
[6] M. Du, Y. Xiao, Y. Geng, Y. Chen, H. Jiang, C. Dong, Q. Guo, Q. Guo, G. Li, E. Zhou, *J. Mater. Chem. C* **2022**, *10*, 10114.
[7] S. Holliday, R. S. Ashraf, A. Wadsworth, D. Baran, S. A. Yousaf, C. B. Nielsen, C.-H. Tan, S. D. Dimitrov, Z. Shang, N. Gasparini, M. Alamoudi, F. Laquai, C. J. Brabec, A. Salleo, J. R. Durrant, I. McCulloch, *Nat. Commun.* **2016**, *7*, 11585.
[8] M. Manceau, S. Chambon, A. Rivaton, J.-L. Gardette, S. Guillerez, N. Lemaître, *Sol. Energy Mater. Sol. Cells* **2010**, *94*, 1572.
[9] K. Tremel, S. Ludwigs, *P3HT Revisited – From Molecular Scale to Solar Cell Devices*, Springer, Berlin **2014**, *265*, 39.
[10] J. Xiao, X. Jia, C. Duan, F. Huang, H.-L. Yip, Y. Cao, *Adv. Mater.* **2021**, *33*, 2008158.
[11] C. Yang, S. Zhang, J. Ren, M. Gao, P. Bi, L. Ye, J. Hou, *Energy Environ. Sci.* **2020**, *13*, 2864.
[12] B. Chang, C.-H. Chen, T.-F. Hsueh, S. Tan, Y.-C. Lin, Y. Zhao, B.-S. Tsai, T.-Y. Chu, Y.-N. Chang, C.-E. Tsai, C.-S. Chen, K.-W. Wei, *ACS Appl. Mater. Interfaces* **2023**, *15*, 52651.
[13] H. Tarikhum B, F. Almyahi, B. Ali, *Karbala Int. J. Mod. Sci.* **2023**, *9*.
[14] J. Bertrandie, J. Han, C. S. P. de Castro, E. Yengel, J. Gorenflot, T. Anthopoulos, F. Laquai, A. Sharma, D. Baran, *Adv. Mater.* **2022**, *34*, 2202575.
[15] B. Yang, Y. Yuan, P. Sharma, S. Poddar, R. Korlacki, S. Ducharme, A. Gruverman, R. Saraf, J. Huang, *Adv. Mater.* **2012**, *24*, 1455.

[16] C. Wöpke, C. Göhler, M. Saladina, X. Du, L. Nian, C. Greve, C. Zhu, K. M. Yallum, Y. J. Hofstetter, D. Becker-Koch, N. Li, T. Heumüller, I. Milekhin, D. R. T. Zahn, C. J. Brabec, N. Banerji, Y. Vaynzof, E. M. Herzig, R. C. I. MacKenzie, C. Deibel, *Nat. Commun.* **2022**, *13*, 3786.
[17] L. Perdigón-Toro, Q. Le Phuong, F. Eller, G. Freychet, E. Saglamkaya, J. I. Khan, Q. Wei, S. Zeiske, D. Kroh, S. Wedler, A. Köhler, A. Armin, F. Laquai, E. M. Herzig, Y. Zou, S. Shoaee, D. Neher, *Adv. Energy Mater.* **2022**, *12*, 2103422.
[18] M. Gao, Y. Liu, K. Xian, Z. Peng, K. Zhou, J. Liu, S. Li, F. Xie, W. Zhao, J. Zhang, X. Jiao, Xuechen, L. Ye, *Aggregate* **2022**, *3*, e190.
[19] C. Yang, R. Yu, C. Liu, H. Li, S. Zhang, J. Hou, *ChemSusChem* **2021**, *14*, 3607.
[20] C. Yang, S. Zhang, J. Hou, *Aggregate* **2022**, *3*, e111.
[21] F. Eller, F. A. Wenzel, R. Hildner, R. W. A. Havenith, E. M. Herzig, *Small* **2023**, *19*, e2207537.
[22] L. Di Mario, D. Garcia Romero, M. J. Pieters, F. Eller, C. Zhu, G. Bongiovanni, E. M. Herzig, A. Mura, M. A. Loi, *J. Mater. Chem.* **2023**, *11*, 2419.
[23] S. M. Hosseini, N. Tokmoldin, Y. W. Lee, Y. Zou, H. Y. Woo, D. Neher, S. Shoaee, *Sol. RRL* **2020**, *4*, 2000498.
[24] W. Wang, L. Song, D. Magerl, D. Moseguí González, V. Körstgens, M. Philipp, J.-F. Moulin, P. Müller-Buschbaum, *Adv Funct Mater* **2018**, *28*, 1800209.
[25] J. Gao, J. D. Roehling, Y. Li, H. Guo, A. J. Moulé, J. K. Grey, *J. Mater. Chem. C* **2013**, *1*, 5638.
[26] I. E. Jacobs, E. W. Aasen, J. L. Oliveira, T. N. Fonseca, J. D. Roehling, J. Li, G. Zhang, M. P. Augustine, M. Mascal, A. J. Moulé, *J. Mater. Chem. C* **2016**, *4*, 3454.
[27] I. E. Jacobs, C. Cendra, T. F. Harrelson, Z. I. Bedolla Valdez, R. Faller, A. Salleo, A. J. Moulé, *Mater. Horiz.* **2018**, *5*, 655.
[28] L. Müller, D. Nanova, T. Glaser, S. Beck, A. Pucci, A. K. Kast, R. R. Schröder, E. Mankel, P. Pingel, D. Neher, W. Kowalsky, R. Lovrincic, *Chem. Mater.* **2016**, *28*, 4432.
[29] S. Guo, W. Wang, E. M. Herzig, A. Naumann, G. Tainter, J. Perlich, P. Müller-Buschbaum, *ACS Appl. Mater. Interfaces* **2017**, *9*, 3740.
[30] S. Dong, T. Jia, K. Zhang, J. Jing, F. Huang, *Joule* **2020**, *4*, 2004.
[31] X. Dong, Y. Jiang, L. Sun, F. Qin, X. Zhou, X. Lu, W. Wang, Y. Zhou, *Adv Funct Mater* **2022**, *32*, 2110209.
[32] Y. Minami, A. Hoshino, Y. Higuchi, M. Hamaguchi, Y. Kaneko, Y. Kirita, S. Taminishi, T. Nishiji, A. Taruno, M. Fukui, Z. Arany, S. Matoba, *Nat. Commun.* **2023**, *14*, 1870.
[33] M. A. Ruderer, S. Guo, R. Meier, H.-Y. Chiang, V. Körstgens, J. Wiedersich, J. Perlich, S. V. Roth, P. Müller-Buschbaum, *Adv Funct Mater* **2011**, *21*, 3382.
[34] K. Feng, D. Zhang, F. Liu, H. Li, J. Xu, Y. Xia, Y. Li, H. Lin, S. Wang, M. Shao, Z. Kang, J. Zhong, *Adv. Energy Mater.* **2020**, *10*, 1904234.
[35] K. Herrmann, S. Freund, F. Eller, T. Rößler, G. Papastavrou, E. M. Herzig, M. Retsch, *Materials* **2022**, *15*, 7700.
[36] J. Clark, C. Silva, R. H. Friend, F. C. Spano, *Phys. Rev. Lett.* **2007**, *98*, 206406.
[37] J. Gierschner, Y.-S. Huang, B. van Averbeke, J. Cornil, R. H. Friend, D. Beljonne, *J. Chem. Phys.* **2009**, *130*, 44105.
[38] A. Köhler, H. Bässler, *Electronic Processes in Organic Semiconductors. An Introduction*, Wiley-VCH GmbH, Weinheim, Germany, **2022**.
[39] C. A. Sandstedt, R. D. Rieke, C. J. Eckhardt, *Chem. Mater.* **1995**, *7*, 1057.
[40] F. C. Spano, *J. Chem. Phys.* **2005**, *122*, 234701.
[41] F. C. Spano, C. Silva, *Annu. Rev. Phys. Chem.* **2014**, *65*, 477.
[42] S. Pröller, F. Liu, C. Zhu, C. Wang, T. P. Russell, A. Hexemer, P. Müller-Buschbaum, E. M. Herzig, *Adv. Energy Mater.* **2016**, *6*, 066101.
[43] Y. Qin, Y. Xu, Z. Peng, J. Hou, H. Ade, *Adv Funct Mater* **2020**, *30*, 2005011.
[44] D. Kroh, F. Eller, K. Schötz, S. Wedler, L. Perdigón-Toro, G. Freychet, Q. Wei, M. Dörr, D. Jones, Y. Zou, E. M. Herzig, D. Neher, A. Köhler, *Adv Funct Mater* **2022**, *32*, 2205711.
[45] S. Pröller, D. Moseguí González, C. Zhu, E. Schaible, C. Wang, P. Müller-Buschbaum, A. Hexemer, E. M. Herzig, *Rev. Sci. Instrum.* **2017**, *88*, 66101.
[46] J. Clark, J.-F. Chang, F. C. Spano, R. H. Friend, C. Silva, *Appl. Phys. Lett.* **2009**, *94*, 163306.
[47] C. Scharsich, R. H. Lohwasser, M. Sommer, U. Asawapirom, U. Scherf, M. Thelakkat, D. Neher, A. Köhler, *J Polym Sci B Polym Phys* **2012**, *50*, 442.
[48] F. M. Keheze, D. Raithel, T. Wu, D. Schiefer, M. Sommer, R. Hildner, G. Reiter, *Macromolecules* **2017**, *50*, 6829.
[49] F. C. Spano, *Chem. Phys.* **2006**, *325*, 22.
[50] E. Gann, T. Crofts, G. Holland, P. Beaucage, T. McAfee, R. J. Kline, B. A. Collins, C. R. McNeill, D. A. Fischer, D. M. DeLongchamp, *J. Phys.: Condens. Matter* **2021**, *33*, 164001.